Ultrafast reversal of the ferroelectric polarization

R. Mankowsky[1], A. von Hoegen[1], M. Först[1], A. Cavalleri[1,2]

[1]*Max Planck Institute for the Structure and Dynamics of Matter, 22761 Hamburg, Germany.*
[2]*Department of Physics, University of Oxford, Clarendon Laboratory, Oxford OX1 3PU, UK.*

The ability to manipulate ferroelectrics at ultrafast speeds has long been an elusive target for materials research. By using short optical pulses to coherently displace all atoms along the ferroelectric mode, switching times could be shortened by two orders of magnitude compared to what is possible with pulsed electric fields. Here, we report on the demonstration of ultrafast optical reversal of the ferroelectric polarization in $LiNbO_3$. Rather than driving the ferroelectric mode directly, we couple to it indirectly by exciting an auxiliary high-frequency vibration. The ferroelectric polarization is then reversed due to the anharmonic coupling between the two modes, as revealed by time-resolved, phase-sensitive second-harmonic generation. Reversal can be induced in both directions, a key pre-requisite for practical applications.

The ferroelectric polarization is typically controlled with static or pulsed electric fields. Switching is in this case an incoherent process, with speed limited to hundreds of picoseconds [1,2,3] by the nucleation and growth of oppositely polarized domains. To overcome these limitations, attempts have been made to drive the ferroelectric mode coherently with light pulses. These strategies, which have been based either on impulsive Raman scattering [4,5,6,7] or direct excitation of the ferroelectric mode [8,9,10] at THz frequencies, have not yet been completely successful.

Recent theoretical work [11] has analyzed an alternative route to manipulate the ferroelectric polarization on ultrafast timescales. It has been proposed that a coherent displacement of the ferroelectric mode could be achieved indirectly, by exciting a second, anharmonically-coupled vibrational mode at higher frequency. The underlying mechanism, discussed more comprehensively in supplementary section 1, is captured by the following minimal model. Consider (see also Figure 1) a double well energy potential along the ferroelectric mode coordinate Q_P

$$V_P\left(Q_P\right)=-\frac{1}{2}\omega_P^2 Q_P^{\,2}+\frac{1}{4}c_p Q_P^4,$$

where ω_p is the frequency of the ferroelectric mode for a fixed temperature $T < T_C$. Take then a second mode Q_{IR} with frequency ω_{IR}, which is anharmonically coupled to the ferroelectric mode with a quadratic-linear dependence of the interaction energy $aQ_{IR}^2 Q_P$:

$$V\left(Q_P,Q_{IR}\right)=V_P\left(Q_P\right)+\frac{1}{2}\omega_{IR}^2 Q_{IR}^2-aQ_{IR}^2 Q_P$$

For periodic driving Q_{IR}, most naturally by a mid-infrared light pulse, the dynamics of the two modes is described by the following equations of motion

$$\ddot{Q}_{IR} + \gamma_{IR}\dot{Q}_{IR} + \omega_{IR}^2 Q_{IR} = 2aQ_P Q_{IR} + f\left(t\right),$$

$$\ddot{Q}_P + \gamma_P \dot{Q}_P - \omega_P^2 Q_P + c_P Q_P^3 = aQ_{IR}^2,$$

where $f\left(t\right) = A\sin\left(\omega_{IR}t\right)\cdot\exp\left(-4t^2/T^2\right)$ is the driving pulse with Gaussian envelope of duration T and frequency ω_{IR}. The driven coordinate Q_{IR} experiences oscillations about its equilibrium position, whereas the ferroelectric mode Q_P is subject to a unidirectional force $\partial V/\partial Q_P = aQ_{IR}^2$ [12,13]. A similar conversion of driven oscillatory motions into directional displacements has been previously demonstrated in a number of non-ferroelectric materials [14,15,16].

A solution of these two coupled equations of motion is displayed in the lower panel of Figure 1b. Two regimes are found. For small oscillation amplitudes in Q_{IR}, the double well potential undergoes a prompt displacement, launching oscillations of Q_P around a new position. In this case, the material retains at all times the sign of the equilibrium polarization, which is not reversed. For oscillation amplitudes of Q_{IR} in excess of a specific threshold, the model predicts that the polarization is switched toward the neighboring well.

Here, we seek to validate these ideas experimentally for the case of $LiNbO_3$, a rhombohedrally distorted perovskite ferroelectric with Curie temperature T_C = 1210°C. Below T_C, the Li and Nb sublattices move toward the oxygen octahedra, inducing a stable electrical polarization along the c axis. The ferroelectric mode (see Figure 1a for a schematic of the atomic displacements) is strongly coupled to a second, high frequency (ω_{IR} = 19 THz) mode of A_1 symmetry Q_{IR} (Ref. 11).

We excited this A_1 mode in a 5-mm thick x-cut single-domain $LiNbO_3$ crystal using 150-fs mid-infrared pulses at 19 THz frequency. The pump pulses were obtained by optical parametric amplification and difference frequency generation. The penetration depth of the mid-infrared pulses was 3.2μm. The polarization dynamics were measured by recording the second harmonic (SH) signal generated by a 35-fs, 800-nm-wavelength probe pulse, which was delayed in time with respect to the excitation (supplementary section 2 for details).

Pump induced changes in the SH intensity $I_{SH} \propto \left| \varepsilon_0 \chi^{(2)} \cdot E^2_{\text{Probe}}(t) \right|^2$ yielded the magnitude of the time dependent second order susceptibility $\chi^{(2)}$, which is directly proportional to the polarization P_S [17]. Higher order contributions near the second harmonic frequency $2\omega_{probe}$, most notably those descending from cubic $\chi^{(3)}$ nonlinearities at frequencies $2\omega_{probe} + \omega_{MIR}$ and $2\omega_{probe} - \omega_{MIR}$, were filtered away spatially (as described in supplementary section 3).

For excitation at fluences F < 50 mJ/cm^2, we observed a reduction in SH intensity to a finite value within 200 fs after optical excitation. As predicted by the model of Figure 1, we observed a rapid exponential recovery and coherent oscillations at 16 THz, which we attribute to a phonon-polariton mode [18,19] associated with the driven A_1 phonon (see Figure 2).

For fluences above a threshold value of 60 mJ/cm^2 up to the maximum fluence possible in our setup (95 mJ/cm$^{2)}$, the second harmonic intensity was observed to vanish completely after approximately 200 fs, recover to a finite value, and then vanish again, before relaxing back to the equilibrium state.

The nature of this “double-dip” dynamics was studied by measuring the phase of the second harmonic electric field, in addition to its modulus reported in Figure 2. To obtain these phase-

resolved dynamics, we interfered the time dependent second harmonic signal reported in Figure 2 with a reference second harmonic pulse generated in a non-excited crystal (see Figure 3 and supplementary information section 3). The resulting interference pattern consisted of a set of fringes, whose changes in spatial position reflected the changes in phase of the second harmonic signal generated in the driven $LiNbO_3$ crystal.

Figure 3b displays the time dependent interference signal integrated along the fringe direction for the maximum pump fluence of 95 mJ/cm^2. The plot shows a constant phase for the first 200 fs following excitation, during which the SH intensity reduces. As the intensity reached zero, the phase of the interference pattern was observed to suddenly switch by 180°. The phase remained constant until the "second dip" occurred at 200 fs time delay, when the phase switched back to the initial value.

Thus, for time delays between 0 fs and 200 fs the polarization was transiently reversed.

A deeper understanding of the reversal process was obtained by analyzing the time dependent changes in SH intensity for different probe polarizations. As shown in Figure 4, the polarization dependence of the second harmonic retained the same symmetry and shape of that observed at equilibrium for all time delays. Hence, the dynamical reversal occurs only along the c axis with no rotations in the plane, consistent with the minimal model presented in Figure 1.

We also tested a second prediction of the model. As the interaction term is quadratic in Q_{IR} and linear in Q_P, one expects that oscillatory motions of the driven infrared mode lead to a force with sign that depends on the initial equilibrium polarization state. For a polarization pointing "up", the model predicts a force toward the "down" state, and viceversa (Ref. 11). Polarization reversal should then be observed starting from both equilibrium states without changing the pump pulse characteristics. In Figure 5 we present the time dependent

polarization measured from both initial polarization states, as extracted from the second harmonic intensity and phase according to $P_S(\tau)/P_{S,0} = \sqrt{I_{SH}/I_{SH,0}}e^{i\varphi(\tau)} + c.c.$. As predicted, the sign of the polarization could be transiently reversed, with a similar dynamical evolution in the two cases.

Thirdly, the model predicts that polarization reversal should exhibit a threshold. In Figure 6a, we show that for an excitation pulse made resonant with the A_1 mode transverse optical frequency $\omega_{IR,\mathrm{TO}}$ at 19 THz, the polarization reverses only for fluences that exceed 60 mJ/cm^2.

Finally, we expect the reversal to be achieved most effectively when the pump pulse is made resonant with the phonon mode. Indeed, Figure 6a shows that the threshold fluence substantially increased for pump wavelengths detuned from this resonance condition. This pump wavelength dependence is clearly captured also in Figure 6b, in which we plot the slope of Figure 6a, which closely follows the extinction coefficient of $LiNbO_3$, and peaks at $\omega_{IR,\mathrm{TO}}$ (Figure 6b).

Hence, the reversal without rotation, the bi-directional nature of the effect, the existence of a switching threshold and the resonance with the frequency of the infrared mode, all indicate that the essence of this phenomenon is well understood in terms of anharmonic coupling and displacement of the ferroelectric mode.

Some issues remain not well understood. The reversal is found to be of at most 40% of the polarization. This may be due to the limited fluence available with our optical setup (95 mJ/cm^2 at 19 THz). This effect, which is not predicted by the minimal model, may be a sign of spatially inhomogeneous reversal. We envisage new experiments that make use of ultrafast

diffuse x-ray scattering with Free Electron Lasers to quantify the possible inhomogeneity [20].

The second observation that is not understood is the rapid return of the polarization to the initial state. In the model of Figure 1, switching to a stable state is expected when the threshold is exceeded. One explanation may be that the crystal lattice needs to relax along other modes in order to permanently stabilize the reversed state, and this is never achieved because of the short lifetime of the transient reversal. In the methods section we elaborate on this possibility, considering the contribution of more anharmonic terms (see also Extended Data Figure 1). If this is the case, permanent polarization reversal on femtosecond timescales might require selective excitation of additional vibrational modes with separate pulses to facilitate the relaxation. The rapid return to the initial polarization may also be explained by the formation of uncompensated charges after polarization reversal of only a fraction of the material. The use of thin films or other types of fabricated structures that isolate the reversed volume may improve the lifetime or clarify these points.

Despite these limitations, which at the present stage make it impossible to build a non-volatile ultrafast memory unit, immediate applications for the transient polarization reversal demonstrated here can already be envisaged. For example, the ability to reverse the polarization at these speeds may be used to control complex functionalities dynamically in materials that exhibit more than one coupled ferroic order [21,22,23] or to transfer charges at ultrafast speeds across hetero-interfaces [24,25].

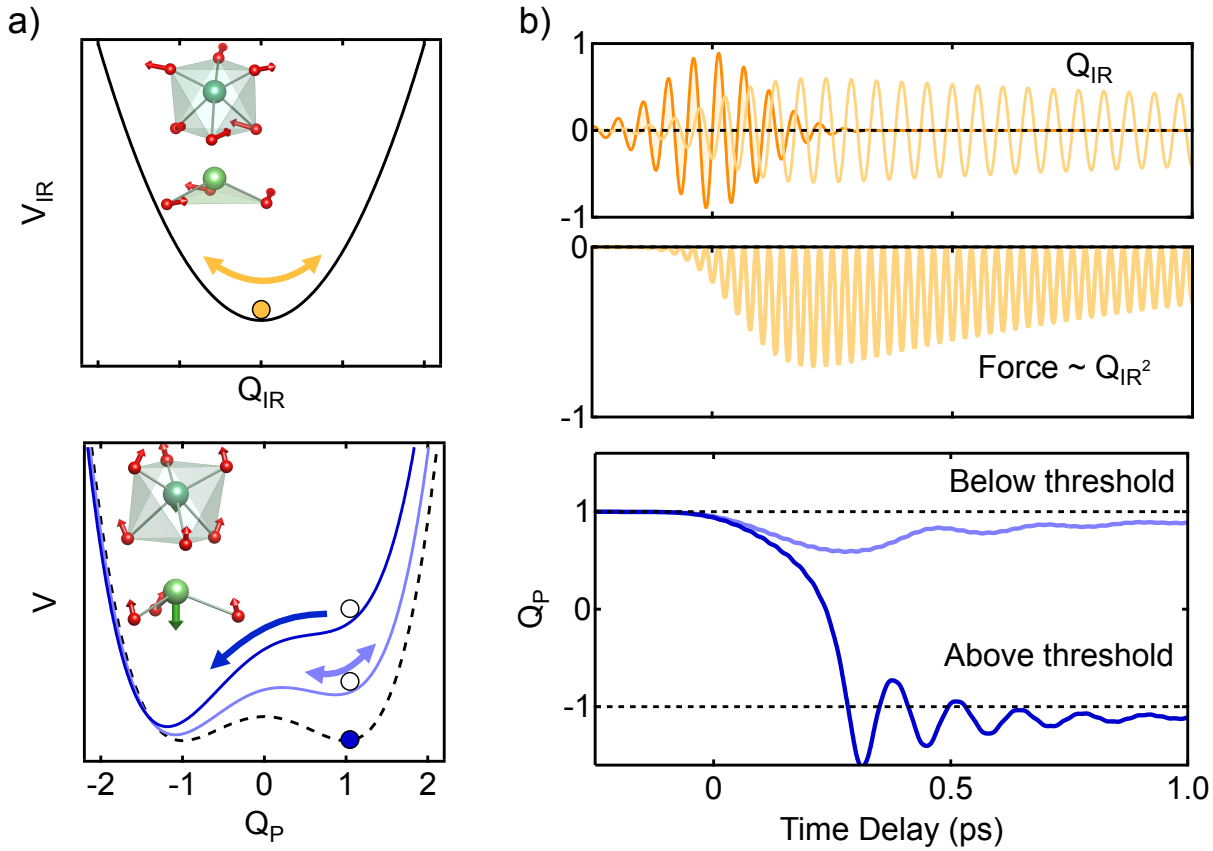

FIG. 1. **a**) Harmonic energy potential of the resonantly excited A_1 mode Q_{IR}. The lower panel shows the double well potential along the ferroelectric mode Q_P. For finite amplitude of Q_{IR}, the energy minimum of the equilibrium potential (dashed line) is first displaced and then destabilized as the amplitude of Q_{IR} exceeds a certain threshold (colored lines). **b**) Corresponding solution to the coupled equations of motion (see text). Following excitation of Q_{IR} with mid-infrared pulses (orange), a force $F \propto Q_{IR}^2$ displaces the ferroelectric mode Q_P toward lower values. For above-threshold excitation of Q_{IR}, the polarization reverses permanently.

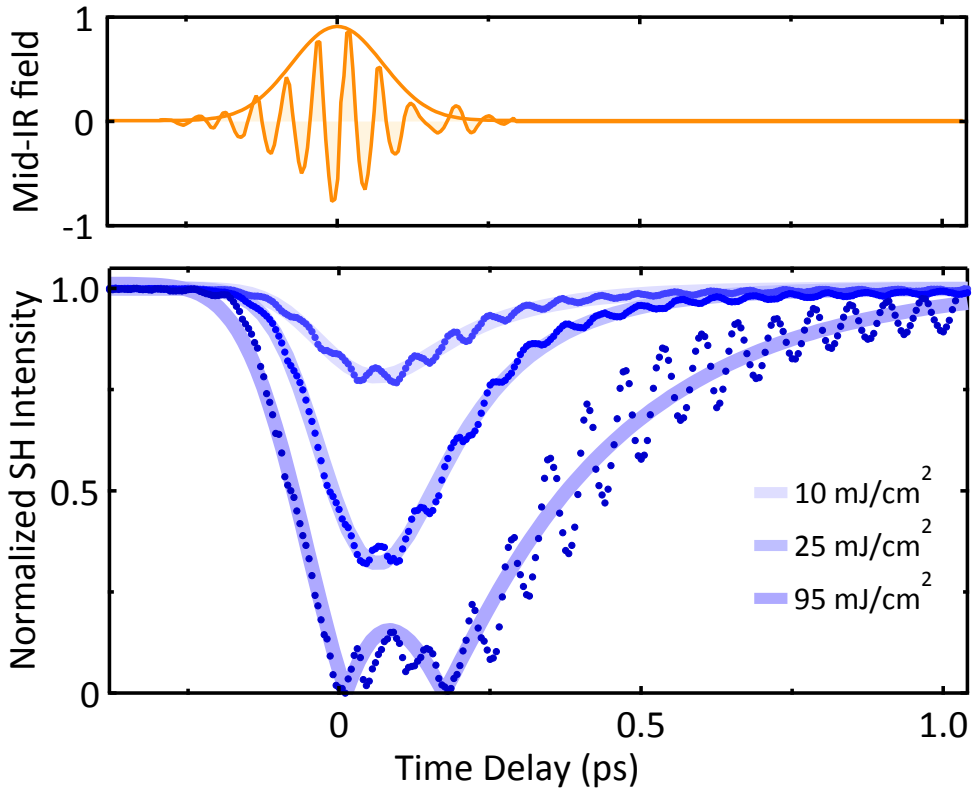

FIG. 2. Normalized second harmonic intensity following resonant excitation of the A_1 mode of Fig. 1a with carrier-envelope phase stable 19 THz mid-infrared pulses. The drop in SH intensity increases with pump fluence. The second harmonic signal vanishes with a double dip structure for all fluences above 60 mJ/cm^2.

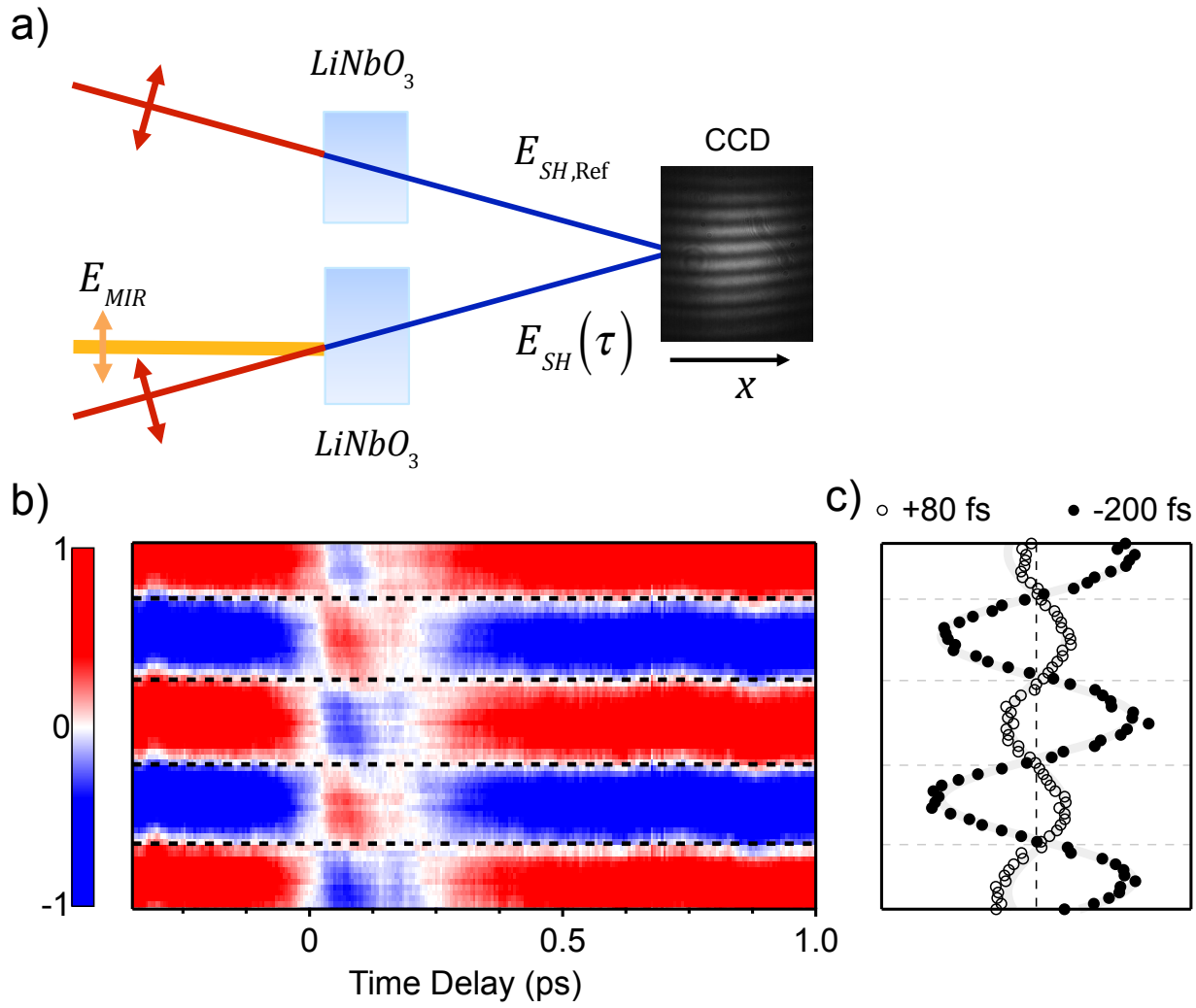

FIG. 3. **a**) Experimental geometry for phase sensitive measurements of the second harmonic. The time dependent second harmonic signal from the excited $LiNbO_3$ crystal is interfered with a reference second harmonic field from an unexcited sample. The interference pattern is recorded with a Charge Coupled Device (CCD) camera. **b**) Time resolved changes of the interference fringes, integrated along the x-axis of the camera, show a transient phase change by 180° (sign reversal) between 0 fs and 200 fs. **c**) Lineouts of the interference pattern at -200 fs and in the reversed polarization state at +80 fs.

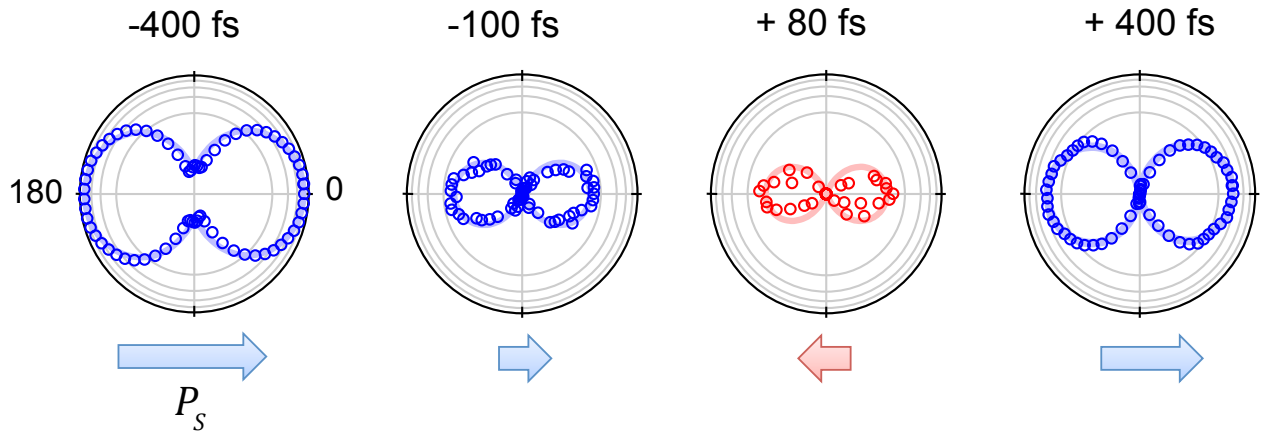

FIG. 4. Probe pulse polarization dependence of the second harmonic signal at four time delays after excitation. The angles 0° and 90° denote a polarization of the 800nm pulses along and perpendicular to the spontaneous polarization. The arrows indicate the time dependent amplitude and sign of the ferroelectric polarization for each time delay, determined from the measurements of Figure 3. The solid lines are fits to the data using the $\chi^{(2)}$ tensor of $LiNbO_3$.

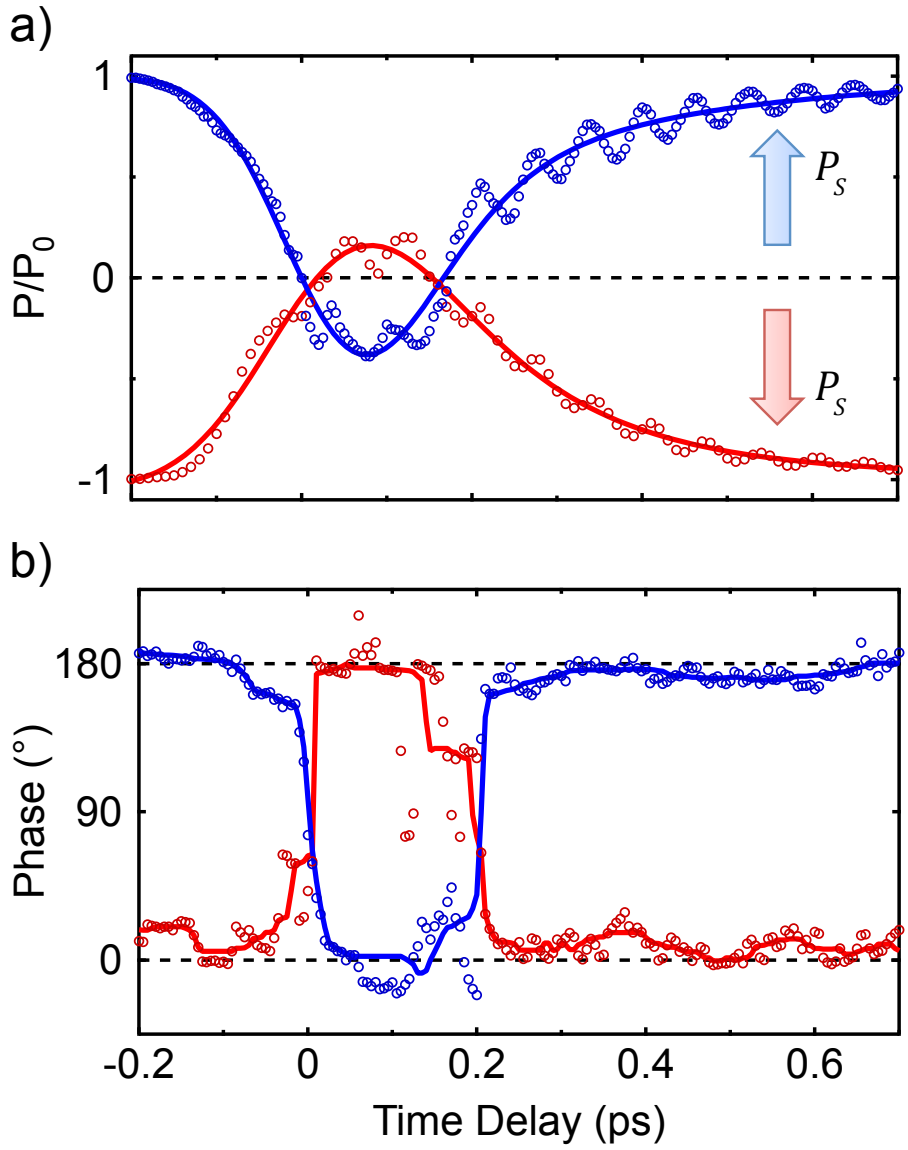

FIG. 5. **a)** Time-resolved changes in the normalized ferroelectric polarization following excitation of $LiNbO_3$ with two opposite initial polarization states, as determined from the measurement of the SH intensity and the phase of the interference pattern. **b)** Phase of the polarization derived from a sine fit to the interference pattern (see text).

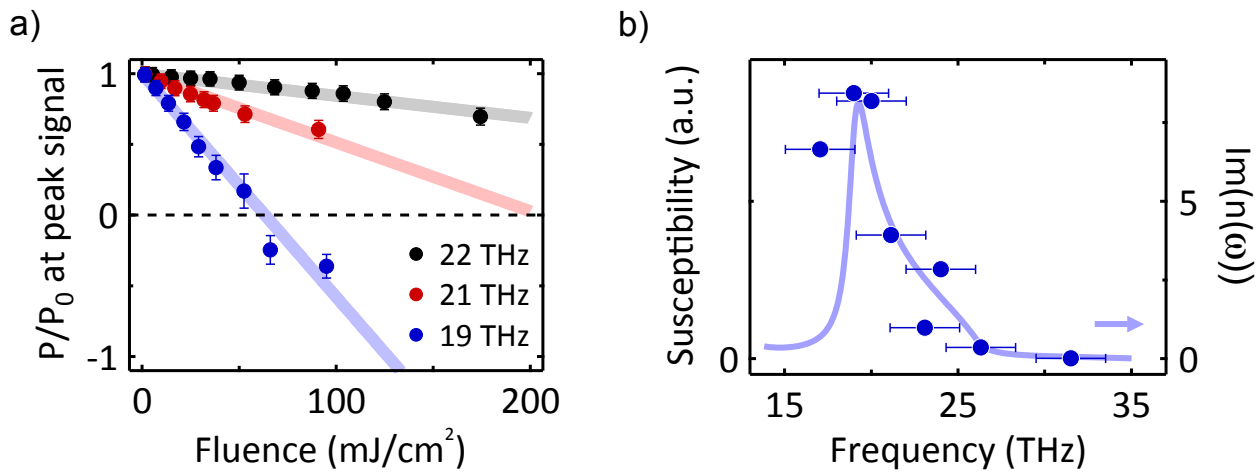

FIG. 6. **a)** Normalized polarization at the peak of the time dependent signal measured as function of pump fluence. The three curves correspond to excitation with pulses at different frequencies. The polarization reverses for excitation above 60 mJ/cm2 with pulses at 19 THz, made resonant with the A_1 mode transverse optical frequency $\omega_{IR,\mathrm{TO}}$ of 19 THz. **b)** Susceptibility to the excitation, defined as the slope of the signal of Figure 6a for different frequencies of the pump pulse.

Acknowledgements:

We thank Michael Fechner, Roberto Merlin and Alaska Subedi for valuable discussions. The research leading to these results received funding from the European Research Council under the European Union's Seventh Framework Programme (FP7/2007-2013)/ERC Grant Agreement no. 319286 (QMAC). Funding from the priority program SFB925 of the German Science Foundation is acknowledged.

References and Notes

[1] R. Landauer, Electrostatic Considerations in $BaTiO_3$ Domain Formation during Polarization Reversal, *J. Appl. Phys.* **28**, 227 (1957).

[2] J. Li, B. Nagaraj, H. Liang, W. Cao, Chi. H. Lee, R. Ramesh, Ultrafast polarization switching in thin-film ferroelectrics, *Appl. Phys. Lett.* **84**, 1174-1176 (2004).

[3] K. Fujimoto, Y. Cho, Nanosecond Switching of Nanoscale Ferroelectric Domains in Congruent Single-Crystal $LiTaO_3$ Using Scanning Nonlinear Dielectric Microscopy, *Japanese Journal of Applied Physics* **43**, 2818-2821 (2004).

[4] S. Fahy, R. Merlin, Reversal of Ferroelectric Domains by Ultrashort Optical Pulses, *Phys. Rev. Lett.* **73**, 1122 (1994).

[5] A. Cavalleri, S. Wall, C. Simpson, E. Statz, D. W. Ward, K. A. Nelson, M. Rini, R. W. Schoenlein, Tracking the motion of charges in a terahertz light field by femtosecond X-ray diffraction, *Nature* **442**, 664 (2006).

[6] J. B. Ciaran, K. A. Nelson, Direct time-resolved measurement of anharmonic lattice vibrations in ferroelectric crystals, *J. Chem. Phys.* **107**, 9691 (1997).

[7] K. Istomin, V. Kotaidis, A. Plech, Q. Kong, Dynamics of the laser-induced ferroelectric excitation in $BaTiO_3$ studied by x-ray diffraction *Appl. Phys. Lett.* **90**, 022905 (2007).

[8] T. Qi, Y.-H. Shin, K.-L. Yeh, K. A. Nelson, A. M. Rappe, Collective Coherent Control: Synchronization of Polarization in Ferroelectric $PbTiO_3$ by Shaped THz Fields, *Phys. Rev. Lett.* **102**, 247603 (2009).

[9] S. Grübel, J. A. Johnson, P. Beaud, C. Dornes, A. Ferrer, V. Haborets, L. Huber, T. Huber, A. Kohutych, T. Kubacka, M. Kubli, S. O. Mariager, J. Rittmann, J. I. Saari, Y. Vysochanskii, G. Ingold, S. L. Johnson, Ultrafast x-ray diffraction of a ferroelectric soft mode driven by broadband terahertz pulses, *arXiv*, 1602.05435 (2016).

[10] F. Chen, Y. Zhu, S. Liu, Y. Qi, H.Y. Hwang, N.C. Brandt, J. Lu, F. Quirin, H. Enquist, P. Zalden, T. Hu, J. Goodfellow, M.-J. Sher, M.C. Hoffmann, D. Zhu, H. Lemke, J. Glownia, M. Chollet, A. R. Damodaran, J. Park, Z. Cai, I.W. Jung, M.J. Highland, D.A. Walko, J. W. Freeland, P.G. Evans, A. Vailionis, J. Larsson, K.A. Nelson, A.M. Rappe, K. Sokolowski-Tinten, L. W. Martin, H. Wen, A.M. Lindenberg, Ultrafast terahertz-field-driven ionic response in ferroelectric $BaTiO_3$, *Phys. Rev. B* **94**, 180104(R) (2016).

[11] A. Subedi, Proposal for ultrafast switching of ferroelectrics using midinfrared pulses, *Phys. Rev. B* **92**, 214303 (2015).

[12] A. Subedi, A. Cavalleri, A. Georges, Theory of nonlinear phononics for coherent light control of solids, *Phys. Rev. B* **89**, 220301 (2014).

[13] R. Mankowsky, M. Först, A. Cavalleri, Non-equilibrium control of complex solids by nonlinear phononics, *Rep. Prog. Phys.* **79**, 064503 (2016).

[14] M. Först, C. Manzoni, S. Kaiser, Y. Tomioka, Y. Tokura, R. Merlin, A. Cavalleri, Nonlinear phononics as an ultrafast route to lattice control, *Nature Physics* **7**, 854 (2011).

[15] M. Först, R. Mankowsky, H. Bromberger, D.M. Fritz, H. Lemke, D. Zhu, M. Chollet, Y. Tomioka, Y. Tokura, R. Merlin, J.P. Hill, S.L. Johnson, A. Cavalleri, Displacive lattice excitation through nonlinear phononics viewed by femtosecond X-ray diffraction, *Solid State Commun.* **169**, 24 (2013).

[16] R. Mankowsky, A. Subedi, M. Först, S.O. Mariager, M. Chollet, H. Lemke, J. Robinson, J. Glownia, M. Minitti, A. Frano, M. Fechner, N. Spaldin, T. Loew, M. Le Tacon, B. Keimer,

A. Georges, A. Cavalleri, Nonlinear lattice dynamics as a basis for enhanced superconductivity in $YBa_2Cu_3O_{6.5}$, *Nature* **516**, 71 (2014).

[17] R. C. Miller, A. Savage, Temperature dependence of the optical properties of ferroelectric $LiNbO_3$ and $LiTaO_3$, *Appl. Phys. Lett.* **9**, 169 (1966).

[18] T. F. Crimmins, N. S. Stoyanov, K. A. Nelson, Heterodyned impulsive stimulated Raman scattering of phonon–polaritons in $LiTaO_3$ and $LiNbO_3$, *The Journal of Chemical Physics* **117**, 2882 (2002).

[19] T. P.Dougherty, G. P.Wiederrecht, K. A. Nelson, Impulsive stimulated Raman scattering experiments in the polariton regime, *J. Opt. Soc. Am. B* **9**, 2179 (1992).

[20] A. Barty, S. Boutet, M. J. Bogan, S. Hau-Riege, S. Marchesini, K. Sokolowski-Tinten, N. Stojanovic, R. Tobey, H. Ehrke, A. Cavalleri, St. Düsterer, M. Frank, S. Bajt, B. W. Woods, M. M. Seibert, J. Hajdu, R. Treusch, H. N. Chapman, Ultrafast single-shot diffraction imaging of nanoscale dynamics, *Nat. Phot.* **2**, 415 (2008).

[21] T. Kimura, T. Goto, H. Shintani, K. Ishizaka, T. Arima, Y. Tokura, Magnetic control of ferroelectric polarization, Magnetic control of ferroelectric polarization, *Nature* **426,** 55 (2003).

[22] J. Wang, J. B. Neaton, H. Zheng, V. Nagarajan, S. B. Ogale, B. Liu, D. Viehland, V. Vaithyanathan, D. G. Schlom, U. V. Waghmare, N. A. Spaldin, K. M. Rabe, M. Wuttig, R. Ramesh, Epitaxial $BiFeO_3$ Multiferroic Thin Film Heterostructures, *Science* **299**, 1719-1722 (2003).

[23] Th. Lottermoser, Th. Lonkai, U. Amann, D. Hohlwein, J. Ihringer, M. Fiebig, Magnetic phase control by an electric field, *Nature* **430** 541 (2004).

[24] C. H. Ahn, S. Gariglio, P. Paruch, T. Tybell, L. Antognazza, J.-M. Triscone, Electrostatic Modulation of Superconductivity in Ultrathin $GdBa_2Cu_3O_{7-x}$ Films, *Science* **284**, 1152 (1999).

[25] H. Yamada, M. Kawasaki, Y. Ogawa, Y. Tokura, Perovskite oxide tricolor superlattices with artificially broken inversion symmetry by interface effects, *Appl. Phys. Lett.* **81**, 4793 (2002).

Supplementary material

1 - Models of the lattice dynamics

In the following section, we compare the model discussed in the manuscript and an extended model, which takes into account also cubic lattice anharmonicities along Q_P, as calculated in Ref. 11.

Considering only the dominant coupling term $aQ_{IR}^2 Q_P$, the response of the crystal lattice to the excitation can be described by the lattice potential energy.

$$V = \frac{1}{2}\omega_{IR}^2 Q_{IR}^2 + \frac{1}{2}\omega_P^2 Q_P^2 + \frac{1}{3}b_P Q_P^3 + \frac{1}{4}c_P Q_P^4 - aQ_{IR}^2 Q_P .$$

Here, $\left(\omega_{IR}, Q_{IR}\right)$ and $\left(\omega_P, Q_P\right)$ denote frequencies and normal coordinates of the directly excited and the nonlinearly coupled ferroelectric mode, respectively. The constants b_P and c_P describe the equilibrium lattice anharmonicities.

The left panels of Figure 1 show the potential energy V along Q_P for both the extended model and the minimal model discussed in the main text. At equilibrium, the double well potential exhibits two stable minima, corresponding to the two polarization states ("up" and "down"). The extended model only displays one minimum (dashed lines). In both models, large amplitude oscillations of the driven mode Q_{IR} dynamically induce a new energy minimum with polarization opposite to the equilibrium. Unlike the minimal model (without cubic term), the extended model predicts a return of the polarization to the initial value as soon as the coherent oscillations of Q_{IR} decay.

This is also reflected in the dynamical response of the modes to the excitation, which is described by the equations of motion

$$\ddot{Q}_{IR} + \gamma_{IR}\dot{Q}_{IR} + \omega_{IR}^2 Q_{IR} = 2aQ_P Q_{IR} + f(t),$$

$$\ddot{Q}_P + \gamma_P \dot{Q}_P + \omega_P^2 Q_P + b_P Q_P^2 + c_P Q_P^3 = aQ_{IR}^2 .$$

The minimal model predicts permanent polarization reversal as the oscillation amplitude of the mode Q_{IR} exceeds a certain threshold. For the extended model polarization reversal is unstable and relaxes back to the initial polarization (see panels on the right hand side in Figure 1).

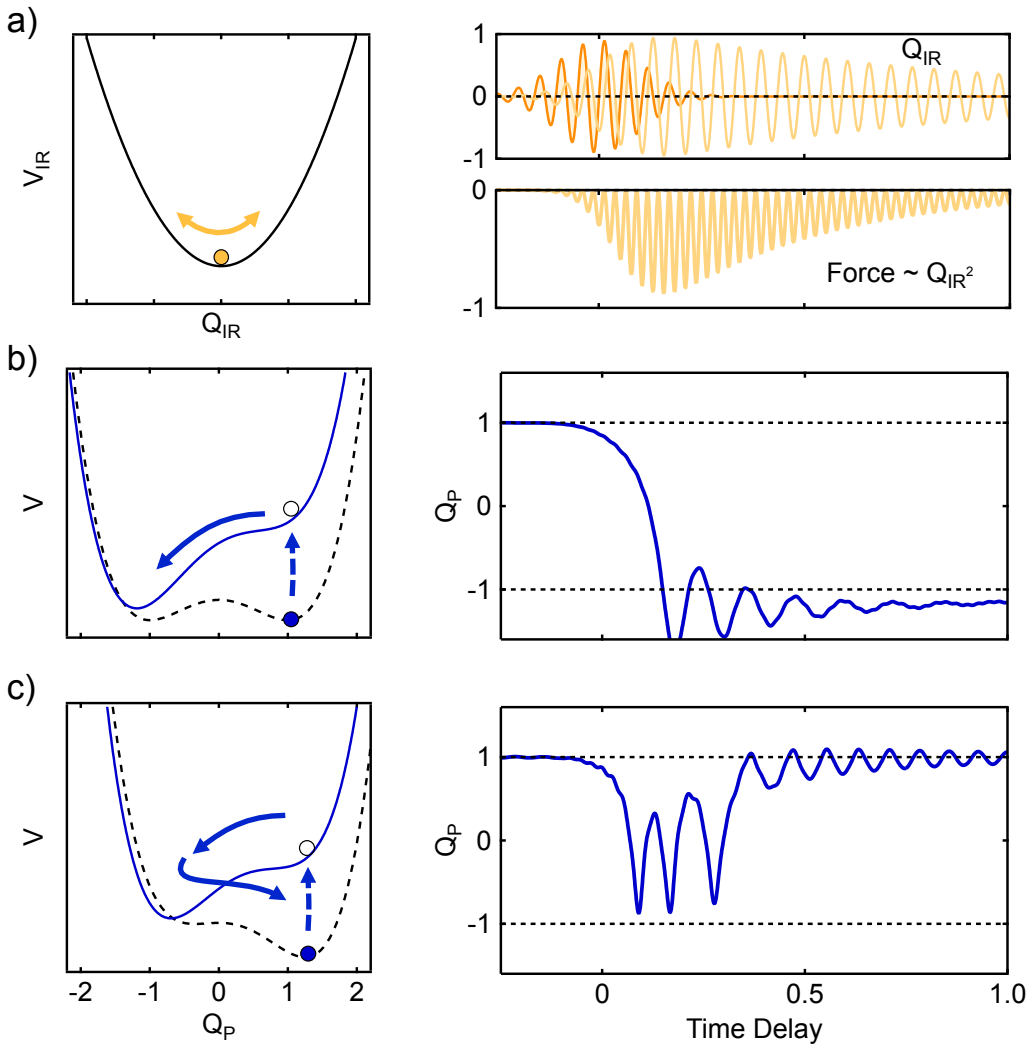

Fig. 1 a) Left: Parabolic energy potential of the resonantly driven infrared-active mode Q_{IR}. Right: Upon excitation with MIR pulses, the atoms start to oscillate in the potential minimum. As described in the main text, due to the coupling term $aQ_{IR}^2Q_P$ a unidirectional force $\partial V / \partial Q_{IR} = aQ_{IR}^2$ displaces the atoms along Q_P toward the state of opposite polarization. **b)** For the minimal model described in the main text, excitation of Q_{IR} to amplitudes above a certain threshold destabilizes the potential minimum, driving the atoms towards the stable state of opposite polarization. **c)** In case of the extended model, the reversed polarization state is only dynamically stabilized as long as IR-active mode Q_{IR} oscillates at large enough amplitude.

Note that the physical situation is not described by either of these models as the coupling to other modes, which is needed to stabilize either polarization state along Q_P are not included.

2 - Second harmonic probing from femtosecond pulses

The sample was a 5 mm thick LBO crystal. The 1/e penetration depth of the electric field of the 19 THz pump electric field, convolved with the spectral bandwidth of 5.5 THz FWHM, was 3.2 μm. In order to trace the polarization dynamics in the excited volume, we detected non phase-matched second harmonic generation from 35-fs 800nm probe pulses, generated in a thin layer below the surface.

This second harmonic signal is the homogenous solution to the wave equation, which results from the discontinuity of the optical properties at the boundary of the crystal [26,27]. The generation occurs in a layer below the surface with thickness given by the SH coherence length of $l_c = 1.27\mu m$, over which the dipole emission builds up constructively [26,28,29]:

$$l_c = \frac{\pi}{\left|k_{2\omega} - 2k_{\omega}\right|} = \frac{\lambda}{4\left|n_{2\omega} - 2n_{\omega}\right|}.$$

This SH pulse, which reflects the polarization dynamics in the pumped volume, propagates with a group velocity determined by the linear optical properties and dispersion of the crystal at 2ω.

In addition to this SH signal, a second pulse with wave vector $2k_{\omega}$ is generated by the fundamental as it propagates through the crystal. This inhomogeneous solution to the wave equation co-propagates both in time and space with the fundamental pulse, therefore with an apparent group velocity determined by the dispersion at ω. Thus, this SH pulse separates both spatially and temporally from the interface-generated SH pulse [27,30] and its intensity is not affected by changes in the excited volume close to the surface (see Figure 2).

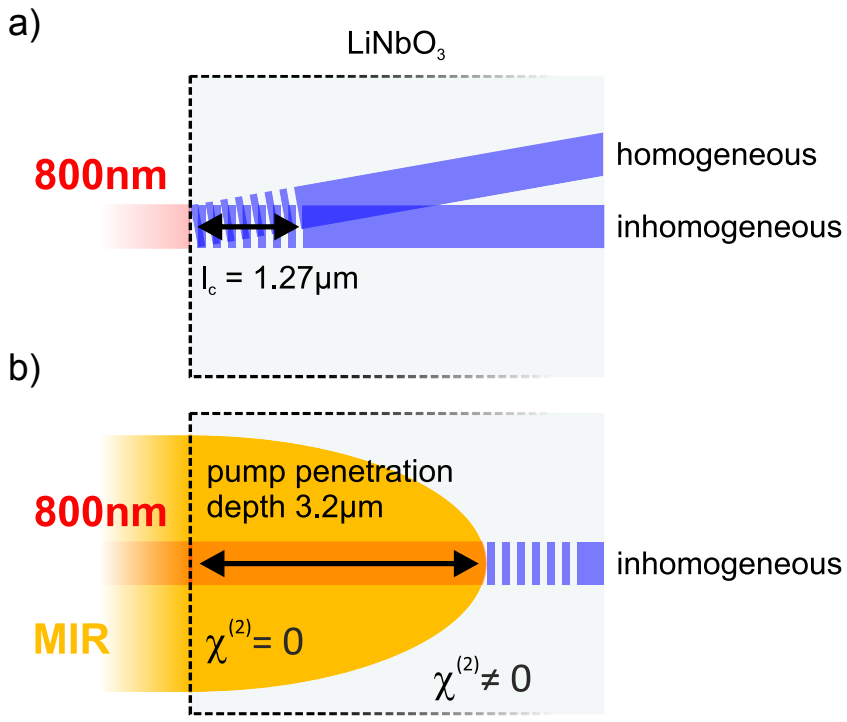

Fig. 2 a) Non phase-matched SH generation in bulk $LiNbO_3$. Two second harmonic signals are generated by the 800nm probe pulses, which separate spatially. The homogeneous solution to the wave equation is generated in a 1.27µm thin layer below the surface. **b)** As the quadratic nonlinearity $\chi^{(2)}$ is depleted within the excited volume, the signal of the homogeneous solution vanishes. In contrast, the SH signal of the inhomogeneous solution is generated in the bulk of the crystal, which is not excited, leaving its intensity unaffected.

These two pulses were separately detected by cross-correlating the total second harmonic radiation emitted from the 5mm thick $LiNbO_3$ crystal, with a synchronized 800-nm pulse in a β-BBO crystal. The measured intensity of the sum frequency is shown in Figure 3 together with a simulation using the SNLO software package (black curve) [31]. The homogeneous solution is delayed by 10.5 ps with respect to the inhomogeneous solution, in good agreement with the simulations. The difference in the relative amplitudes of the homogeneous and inhomogeneous solutions is due to their spatial separation on the detection crystal.

The red curve in Figure 3 shows the same measurement with the sample being excited by the 19 THz MIR pulse at a fixed time delay with respect to the 800 nm pulse. The inhomogeneous solution is almost unaffected due to the limited penetration depth of the MIR pump pulses. In contrast, the homogeneous solution vanishes due to a complete suppression of the optical nonlinearity χ_2 in the excited volume close to the surface. Hence, changes in the excited surface region can be followed by measuring the SH pulses of the homogeneous solution in transmission through the bulk sample.

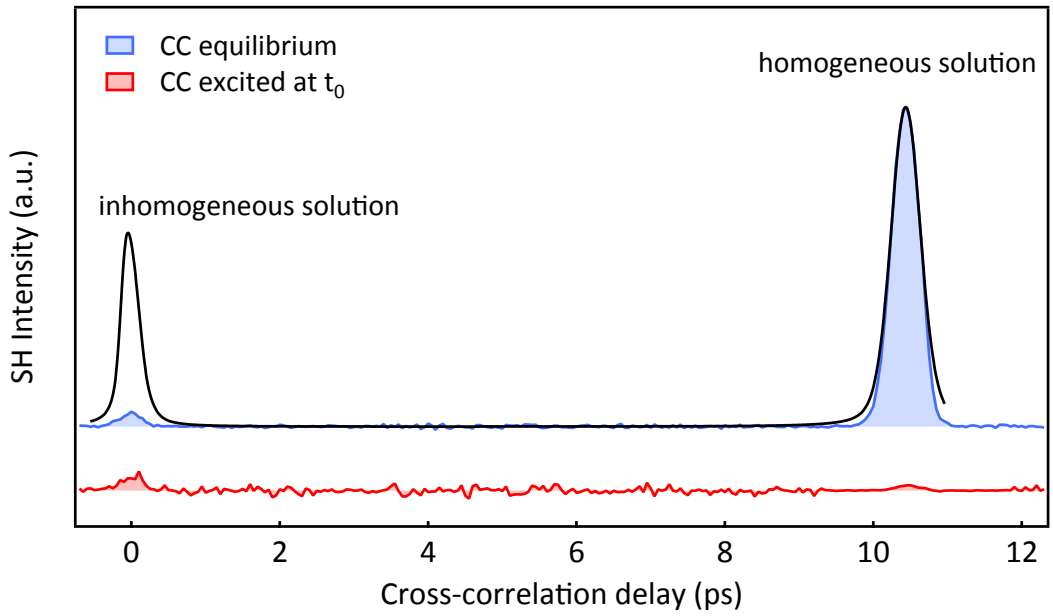

Fig. 3 Cross-correlation between the SH light emitted from the $LiNbO_3$ crystal and a synchronized 800-nm pulse (blue curve). The homogeneous solution to the wave equation, generated at the crystal surface, is delayed by 10.5 ps with respect to the inhomogeneous solution in good agreement with simulations (black line). The excitation of the sample fully suppresses the homogeneous solution while leaving the inhomogeneous unaffected (red curve).

3 - Experimental Setup

Second harmonic intensity measurement

Figure 4 shows the non-collinear pump-probe geometry used in our experiments. An angle of 30° between MIR pump and probe beams was chosen to spatially separate the second harmonic electric fields generated due to quadratic $\chi^{(2)}$ or cubic $\chi^{(3)}$ nonlinearities. The latter process generates a SH field at frequencies $2\omega_{probe} \pm \omega_{MIR}$ by four-wave mixing with the MIR pump pulse, described by the nonlinear polarization

$$P(t) = \varepsilon_0 \chi^{(3)} E^2_{\text{Probe}}(t) \cdot \left(E_{MIR}(t) + c.c. \right).$$

As this interaction involves a momentum transfer, the third-order contribution separates spatially from the second-order contribution.

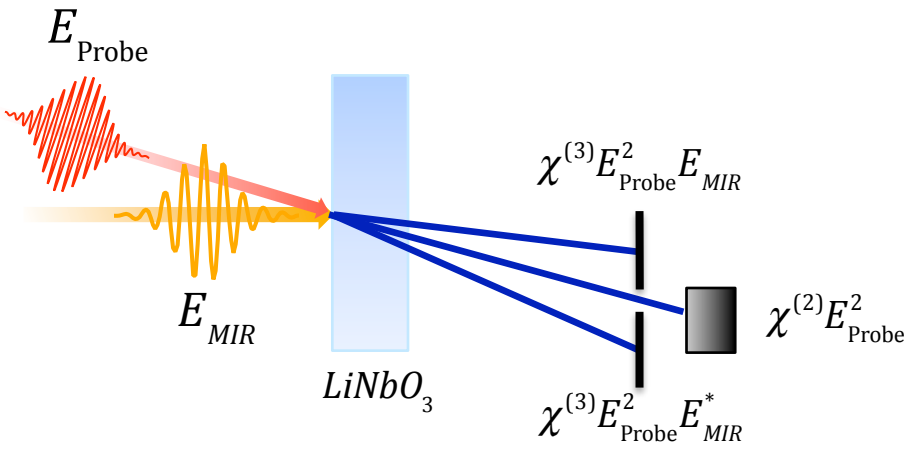

Fig. 4 Sketch of the measurement geometry. The higher order four-wave mixing terms are separated spatially and blocked by a pinhole. The intensity of the remaining second harmonic is then detected with a photomultiplier tube.

Second harmonic phase measurement

The above experimental setup only allows for measuring pump induced changes in the intensity of the SH signal, which holds information on the magnitude of the ferroelectric polarization. To

determine the sign of the polarization, we measured the phase of the emitted SH electric field from the sample at all time delays by interfering it with the SH light generated in a second $LiNbO_3$ crystal. A sketch of the experimental setup is presented in Figure 3a of the main text, showing the measurement of the interference pattern on a CCD-camera. The intensity of an interference fringe at time delay τ between pump and probe pulses is given by

$$I_{SH}(\tau)=\left|E_{SH,\mathrm{Ref}}+E_{SH,0}(\tau)e^{i\varphi(\tau)}\right|^2=I_{SH,\mathrm{Ref}}+I_{SH}(\tau)+2E_{SH,\mathrm{Ref}}\cdot E_{SH,0}(\tau)e^{i\varphi(\tau)}+c.c.,$$

where $E_{SH,\mathrm{Ref}}$ denotes the amplitude of the SH electric field from the reference $LiNbO_3$ crystal and $E_{SH,0}(\tau)e^{i\varphi(\tau)}$ the time-delay dependent amplitude and phase of the SH field from the sample. The interference pattern can be extracted by subtracting the contribution from the terms $I_{SH,\mathrm{Ref}}+I_{SH}(\tau)$, which appear as a Gaussian background along the x and y direction of the CCD. A sine-fit to the residual yields $\varphi(\tau)$ as shown in Figure 5.

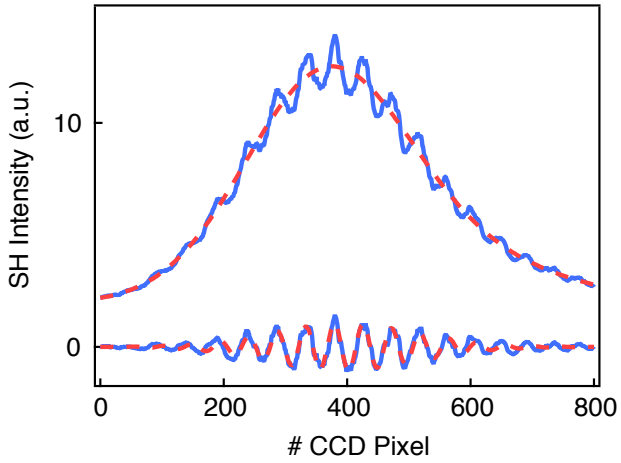

Fig. 5 The time-delay dependent phase of the SH electric field from the sample is obtained by subtracting the Gaussian background from the measured interference pattern and fitting the residual with a sine.

References and Notes:

[26] M. Mlejnek, E. M. Wright, J. V. Moloney, N. Bloembergen, Second Harmonic Generation of Femtosecond Pulses at the Boundary of a Nonlinear Dielectric, *Phys. Rev. Lett*. **83**, 2934 (1999)

[27] V. Roppo, M. Centini, C. Sibilia, M. Bertolotti, D. de Ceglia, M. Scalora, N. Akozbek, M. J. Bloemer, J. W. Haus, O. G. Kosareva, V. P. Kandidov, Role of phase matching in pulsed second-harmonic generation: Walk-off and phase-locked twin pulses in negative-index media, *Phys. Rev. A*. **76**, 033829 (2007)

[28] N. Bloembergen, P. S. Pershan, Light Waves at the Boundary of Nonlinear Media, *Phys. Rev.* **128**, 606 (1962)

[29] P. Schoen, Phase and Polarization Pulse Shaping for Nonlinear Microscopy, *Université Paul Cézanne - Aix-Marseille III*, (2010)

[30] E. Fazio, F. Pettazzi, M. Centini, M. Chauvet, A. Belardini, M. Alonzo, C. Sibilia, M. Bertolotti, M. Scalora, Complete spatial and temporal locking in phase- mismatched second-harmonic generation, *Opt. Exp*. **17**, 3141 (2009)

[31] SNLO nonlinear optics code available from A. V. Smith, AS-Photonics, Albuquerque, NM